POAC'23
Glasgow, United Kingdom

Proceedings of the 27th International Conference on
Port and Ocean Engineering under Arctic Conditions
12-16 June 2023, Glasgow, United Kingdom

SEA SPRAY ICE MICROSTRUCTURE AND BRINE ENTRAPMENT

Sönke Maus[1], Paul Jorrit Rübsamen-von Döhren[1]

[1]Dep. of Civil and Transport Engineering, Norwegian University for Science and Technology, Trondheim, NORWAY, email: sonke.maus@sea-ice.no,

ABSTRACT

Sea spray icing on ships and offshore structures is a major safety concern for operations in polar regions. During a storm a saline ice layer of several centimeter thickness can grow from sea spray within an hour, which can lead to overloading of structures and sinking of ships. The prediction of spray ice growth is still unsatisfying. One considerable uncertainty factor is the freezing process of spray ice. This ice is porous, containing pure ice, air, liquid brine, and to some degree precipitated salts. The amount of brine within the spray ice affects its freezing rate and determines the total load, yet little is known about the brine entrapment process in the ice microstructure. Observations of the latter by magnetic resonance imaging, with spatial resolution of 0.2 to 1 mm, are insufficient for a quantitative description of brine entrapment. We have performed imaging of the microstructure of saline spray ice by X-ray micro-tomography, with a spatial resolution of to 27 to 42 μm. Here we present detailed statistics of the location of salt/brine in sea spray ice as well as pore size distributions of brine pores and drained brine channels in laboratory-grown saline spray ice. The observations suggest that brine is primarily lost through internal drainage channels that are similar to those in sea ice (several millimeter wide) yet formed much faster (within less than an hour compared to days for sea ice). We discuss some implications for modelling the salinity of sea spray ice.

KEY WORDS: Sea spray ice, marine icing, salinity, microstructure, brine channels

INTRODUCTION

Marine icing has been, due to its safety risk for vessels and offshore structures, part of operational weather forecasting for half a century. It is governed by the main processes (i) spray generation (ii) spray flow and hitting of structures and (iii) freezing process of sea spray and their interaction. While models of different complexity have been formulated to predict sea spray icing, their performance is still rather limited. Most of review studies agree that one of the causes for this lack in performance is due to knowledge gaps in the freezing process of sea spray ice and its microstructure. Also when relevant meteorological parameters as well as size and concentration of droplets are known, the freezing of sea spray is a complicated process: crystal growth inside sea spray droplets can be highly nonlinear, depending on boundary conditions and the interaction of thermodynamics and hydrodynamics of saline solutions. Similar to sea ice, the freezing sea spray then forms an agglomerate of crystals, a porous medium with evolving thermodynamic (e.g., density, salinity, temperature, porosity) and mechanical (e.g. strength) properties. Knowledge of these properties is important for evaluating the growth rates of sea spray ice, as well as the loads that icing can build up on ships and offshore structures.

Heat budget of saline ice accretion

The need to know the salinity of sea spray ice is motivated by the fact that sea spray ice may contain considerable amounts of liquid brine. As the heat budget of spray ice is, as for sea ice, dominated by latent heat release, such liquid adds to the load of an ice structure, yet not to the primary heat budget. Heat budget equations of different complexity have been formulated to predict sea spray icing. The simplest prediction model (e.g., Overland et al., 1986) only considers the dependence of ice accretion I (in mass per unit area and time) on the sensible heat flux, which is proportional to the product of wind velocity W and the difference of the temperatures at the ice surface (T_i) and in the air (T_a). The ice mass accretion rate (mass per area and time) may then be approximated as

$$I \approx \frac{C_t W (T_i - T_a)}{L \phi_s}, \tag{1}$$

where C_t is a heat-exchange coefficient (unit $Wm^{-2}s^{-1}$) and L the volumetric latent heat of fusion. As the freezing sea spray ice is saline it contains unfrozen brine, which is accounted for by ϕ_s, the pure ice fraction of the spray ice (while (1-ϕ_s) is the brine volume fraction). The equation neglects specific heat changes during cooling of sea spray, as well as density differences between ice and water/brine. One may then approximate the solid ice fraction as $\phi_s \approx (1 - S_i/S_b)$, where S_b is salinity of brine within the spray ice. S_b is related to T_i through the freezing point relationship. For moderate brine salinities, just a few times the salinity of seawater the latter can be approximated as $T_i \approx -mS_b$[1] and one can write

$$I \approx \frac{C_t W (T_i - T_a)}{L \left(1 - \frac{mS_i}{T_i}\right)}. \tag{2}$$

Equation 2 illustrates the challenge of icing prediction related to two properties of the sea spray ice - salinity S_i and temperature T_i, where the latter has been assumed to be homogeneous within the spray ice. Figure 1a shows this equation for different S_i and T_i in a normalised form, dividing I, by the accretion I_* of ice with zero salinity and T_i at the freezing point of sea water. These curves demonstrate the relevance of ice temperature and salinity for the accretion rate. Figure 1b shows observations of ice salinity versus freezing temperature of drained brine observed by Ono (1964). Unfortunately not many of such observations exist.

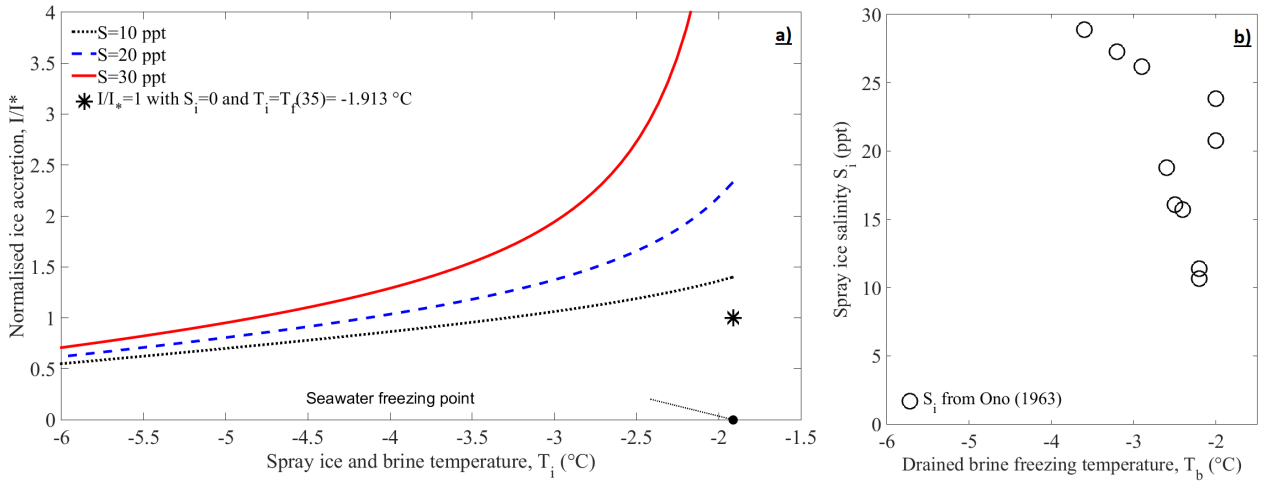

Figure 1: a) Ice accretion rate versus spray ice temperature for $T_a = -10$°C, normalised by $I*$ for ice with zero salinity and T_i at the freezing point of sea water; b) Spray ice salinity versus freezing temperature of drained brine observed by Ono (1964).

[1]With m in the range 0.052 to 0.058 °C/ppt for a temperature between -2 and -8 °C

Spray ice salinity, solid fraction and freezing fraction

For the prediction of S_b (or its equilibrium freezing temperature T_i) and S_i most work to date has followed an approach proposed by Makkonen (1987) to model the salinity S_i of sea spray ice. It is based on the salt balance during accretion of spray ice from incoming sea spray. Let F be the mass flux of sea spray with salinity S_w, I the ice accretion rate with spray ice salinity S_i, and $(F - I)$ the mass of drained brine or not accreting sea spray with salinity S_b. The salt flux balance reads

$$FS_w = IS_i + (F - I)S_b. \tag{3}$$

With $n = I/F$ being the freezing of impinging sea spray that is accreting, this equation may be rearranged to give the salinity S_i of sea spray ice in the form

$$k_{eff} = \frac{S_i}{S_w} = \frac{\dfrac{S_i}{S_b}}{1 - \left(1 - \dfrac{S_i}{S_b}\right) n}. \tag{4}$$

This concept of normalised salinity is analogous to discussion of floating sea ice, where k_{eff} has been termed the *effective solute distribution coefficient* (Weeks and Ackley, 1986). Makkonen (1987) used another formulation from the modelling of sea ice defining the ratio $k = S_i/S_b$ as the *interfacial solute distribution coefficient* at the brine-ice interface. The latter is equivalent to the ice liquid fraction and may may be expressed, by rearranging Eq. 4 further, as

$$k = \frac{S_i}{S_b} = \frac{(1 - n)\dfrac{S_i}{S_w}}{1 - n\dfrac{S_i}{S_w}}. \tag{5}$$

Eq. 3 to 5 extend the heat budget (Eq. 1 and 2) by the salt budget and the freezing fraction $n = I/F$. However, this does not provide a solution for S_i or S_b, but rather specifies the relationship between these salinities and n. If all impinging sea spray is accreting $(n = 1)$, it implies $S_i = S_w$. To proceed with the problem of ice salinity prediction, Makkonen (1987) proposed, in analogy to sea ice modelling, a constant $k = S_i/S_b = 0.26$ and most modelers have since then used a similar value (Dehghani-Sanij et al., 2017). Once k is set, one may use Eq. 4 to calculate k_{eff} (and thus S_i) as a function of n. As this also determines S_b (and thus T_i) one can solve Eq. 1/2. However, the only direct observations of k so far by Ono (1964), derived from collection of brine and simultaneous observations of spray ice salinity, do not support such a constant k yet show a range $0.27 < k < 0.68$ (Figure 2b). In other studies k has not been measured directly yet has been computed on the basis of ice salinity and ice temperature of sampled spray ice (Vefsnmo et al., 1987; Zakrewski and Lozowski, 1987; Ryerson and Gow, 2000; Horjen, 2013). Also these estimates show large scatter and values in the range $0.1 < k < 0.4$. In a laboratory experiment Lock and Foster (1990) found much larger liquid fractions in spray ice grown from saline water, most values corresponding in the range $0.8 < k < 0.5$. As an alternative solution it has been suggested to rather assume a constant $k_{eff} = S_i/S_w = 0.75$ (Lozowski et al., 2000). However, the data from Ono (1964) reproduced in Figure 2a show a range of $0.9 < k_{eff} < 0.3$, with similar observations obtained in later studies (e.g., Ryerson and Gow, 2000; Horjen, 2013).

Hence neither a constant k nor a constant k_{eff} is consistent with observations. It is also worth noting that the work by Ono (1964) is still the only study so far where all the properties in the above Equations (the weights and salinities of ice, brine and sea spray and the ice accretion fraction) have been measured and reported. An interesting result from the latter study is not only the large variability in k and k_{eff}, yet the finding for the ratio $k/k_{eff} = S_w/S_b$ shown in Figure 2, for which a close to linear relationship with the ice accretion fraction is found. At small accretion fraction S_i/S_w approaches one, as one would expect when all sea spray drips off the structure. On the other hand, when all sea spray freezes (I/F=1), the data from Ono show $S_i/S_b \approx 0.5$.

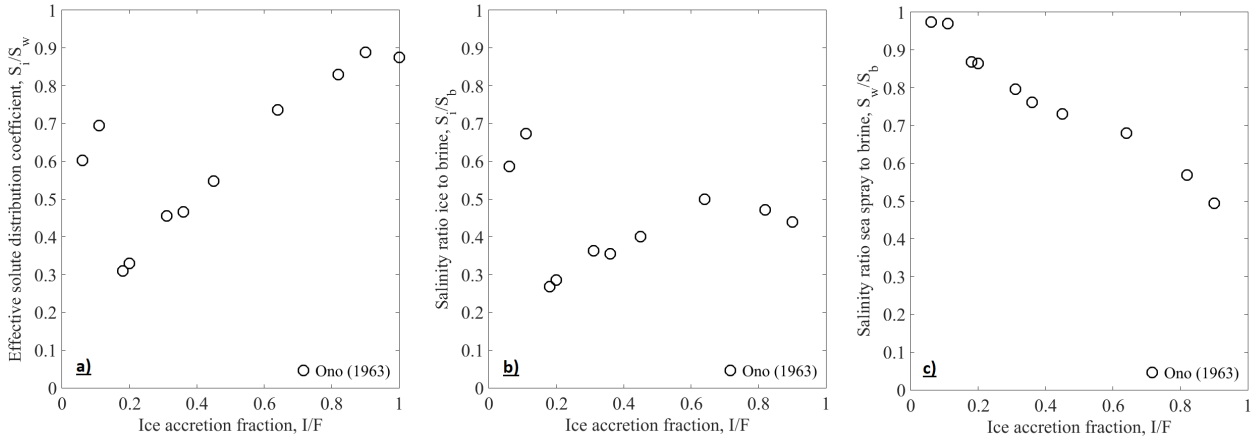

Figure 2: Sea spray ice observations by Ono (1964) versus sea spray accretion fraction: a) effective k_eff; b) ice to brine salinity ratio k; c) sea spray to brine salinity ratio.

Previous work on microstructure of spray ice

The range of observed sea spray ice salinities and ice temperatures (Figure 2) points to the role microstructure plays for brine entrapment. So far this problem has been addressed in two ways. The critical fraction k has been predicted via a dendritic growth model, resulting in a complex dependence of k on growth conditions and spray flux (Blackmore and Lozowski, 1998; Blackmore et al., 2002). However, this model was largely based on data for the growth of dendrites in freshwater, and so far no observations of dendritic structure of sea spray ice exist. Due to rather different liquid fractions obtained during fresh and saline sea spray freezing (Lock and Foster, 1990), it is not clear if the model correctly parametrizes the microstructure and brine entrapment. A physically more consistent formulation for dendritic freezing of saline water on a substrate has been recently suggested by Kong and Liu (2018). It proposes an approach in the lines of morphological stability theory from Mullins and Sekerka (1964), similar to what has been demonstrated for sea ice (Maus, 2020). The second widely accepted model concept is the prediction of brine flow and thermodynamics at the surface of spray ice to constrain the freezing fraction I/F (Blackmore and Lozowski, 1998; Blackmore et al., 2002; Horjen, 2013; Kulyakhtin and Tsarau, 2014).

On the observational side there has been little validation of the model concepts (dendritic growth and brine layer flow). Observations of brine film morphology and flow are lacking. Ono (1964) showed 2D thin section images of sea spray ice, noting that the existence of ice lamella similar to sea ice. In later work more thin section images have been published (Makkonen, 1984; Sackinger et al., 1987), with the most detailed report so far by Ryerson and Gow (2000). The latter authors described the microstructure of ice accreted on different horizontal and USCGC Midgett along with differences in ice salinity and temperature. However quantitative relationships between microstructure characteristics and observed k or k_{eff} were not reported. In a more recent Magnetic Resonance study the 3-d brine channel structure was demonstrated to be a striking feature of spray ice and its desalination. While this study has remained quantitative, possibly due to the limited spatial resolution ($\approx$ 0.2 mm), it clearly points to the role of internal brine channels for the salt budget of sea spray ice. Further support for this hypothesis comes from observations of decreasing spray ice salinity with time (Kulyakhtin, 2014).

The present work presents first results from 3D imaging of the internal microstructure of saline spray ice to better understand its desalination and salinity evolution. We performed non-destructive imaging by X-ray computed micro-tomography (micro-CT) which has become the method of choice to unravel the 3D microstructure and physics of porous media (Desrues et al., 2006; Cnudde and Boone, 2013), and is increasingly used to characterise the microstructure of sea ice (Pringle et al., 2009; Maus et al., 2021; Salomon et al., 2021). We focus on results of imaging with moderate spatial resolution (27 and 42 μm voxel size) to discuss the microstructure of brine channels described by (Ozeki et al., 2005), and the role that these features play in controlling the salinity of sea spray ice.

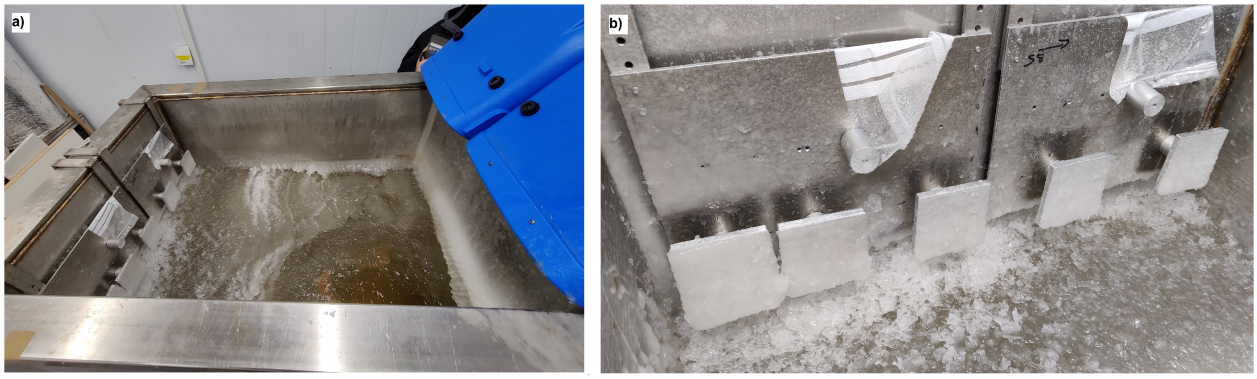

Figure 3: View of the tank at the end of a spray ice experiment after about 2 hours: a) side view showing the position of the (blue) fans on the right, the ice tank filled with slush; b) 5 ice sample holders with 1 -2 cm of spray ice grown.

Sea spray ice was created in a cold laboratory at NTNU with the setup shown in Figure 3. Two strong fans were directed were directed on the surface of a tank with 1.2 x 0.8 m surface exposure and 0.9 m water depth, filled with saline water of salinity 32-35 ‰ NaCl by weight. The air flow hits the water surface with 10-15m/s velocity and at an angle of about 45 degrees.When the generated sea spray hits the back wall of the tank, it freezes onto alumina sample plates of different size (2, 6, 9, 12 cm, and the 40 cm large plate on which the small samples are mounted. Experiments are performed with room temperatures of -7 to -15 °C and a water temperature close to the freezing point of -2 °C. Experiments were normally run for two hours, which is the time it takes for the ice tank to be covered with grease ice. Dependent on temperature, wind speed, and plate location, this typically allows for 0.5-4 centimeters of spray ice growth, corresponding to natural growth rates. The fans are then turned of to let the samples equilibrate to the air temperature within 20 to 30 minutes. Samples are then either removed manually, or they were removed from the plates through a mechanical adhesion test, for which results are presented in a companion paper of these proceedings (Rübsamen-von Döhren et al., 2023). After cutting the samples into suitable sizes, micro-CT imaging was performed at the final sample temperatures.

X-ray microtomographic imaging

Micro-CT scanning was performed within a few hours after the sea spray experiment, and at the final temperature between -7 and -15 °C. To do so spray ice samples were set into passive cooling boxes, kept at the respective temperature by eutectic cooling elements, and carried (5 minutes walk) from the ice laboratory to the micro-CT laboratory. Imaging, segmentation and analysis follows our procedures as applied to sea ice (Maus et al., 2021) and saline ice layers on concrete (Maus et al., 2023) and is shortly described as follows. Scanning was was conducted at the Norwegian Centre for X-ray Diffraction, Scattering and Imaging at NTNU, with an XT H 225 ST micro-CT system from Nikon Metrology NV, equipped with a Perkin Elmer 1620 detector with a 2048 x 2018 pixel field of view. Image acquisition settings were slightly dependent on sample volume, with a current source in the range 90-110 μA and an acceleration voltage of 400-450 kV using a Wolfram target. Scans were performed with 3142 rotation per 360 °C and an exposure time of 708.00 ms (scan duration 40 minutes). The field of view was 54 and 85 mm corresponding to a pixel size of 27 and 42 μm. Specimen were placed in an alumina sample holder with 1-1.5 mm wall thickness. The top and bottom temperature of the sample holder was controlled by a self-assembled cooling system, based on thermo-electric assemblies (www.lairdtech.com), with a precision of 0.5 °C.

Nikon Metrology XT Software was used for reconstruction of the data sets. Data were stored as 16-bit grey value stacks. We used the software GeoDict (GeoDict, 2012-2022) for segmentation into the constituents air, brine and ice, and for determination of several porosity and pore size metrics. Figure 4 shows a photography of a sea spray ice sample (a) and example images in 3D

Table 1: Summary of 3D sample statistics

Plate size	thickness cm	T_a °C	S_i ‰	T_i °C	$\phi_{a,op}$ %	ϕ_b %	$\phi_{a,cl}$ %	$D_{a,op}$ μm	$D_{b,op}$ μm	$D_{b,cl}$ μm	ΔS ‰	$\Delta S_{a,op}$ ‰
3 cm	1.3-1.7	-10	26.2		0.5	15.9	0.44	146 (843)	41	67	7.8	0.06
6 cm	1.8-2.0	-10	23.2		0.9	14.1	0.44	820 (1763)	41	86	10.8	0.5
12 cm	1.5-2.1	-10	22.6		1.3	13.7	0.72	801 (1090)	43	51	11.4	0.6
Large	3.0-4.5	-10	16.2	-5.5	7.9	9.6	0.06	849 (1478)	70	90	17.8	7.8

(b) as well as 3 cross sectional views (c). The yellow ring in the horizontal cross section (upper left) is the alumina sample holder. Air porosity, with much larger contrast to ice, was segmented as described in Maus et al. (2021). Segmentation between brine and ice is more challenging due to the much smaller absorption contrast. We set the histogram threshold between brine and ice to match the theoretical brine porosity that is expected from temperature and salinity. As the smallest pores remain undetected, our median pore sizes are overestimates and only resemble the pores larger than 27 (42) μm. Pore and ice structure sizes were then determined with the PoroDict package of GeoDict (GeoDict, 2012-2022), by a sphere fitting algorithm to determine the fraction of the pore or ice space that belongs to a certain diameter interval. The results from this analysis are the median *brine pore size* D_b and the median *air pore size* D_a, distinguishing further between open and closed pores (subscripts $_{op}$ and $_{cl}$). The pixel size of 27 μm (42 μm for the largest sample presented here) is considered as the uncertainty of all microstructure measures presented.

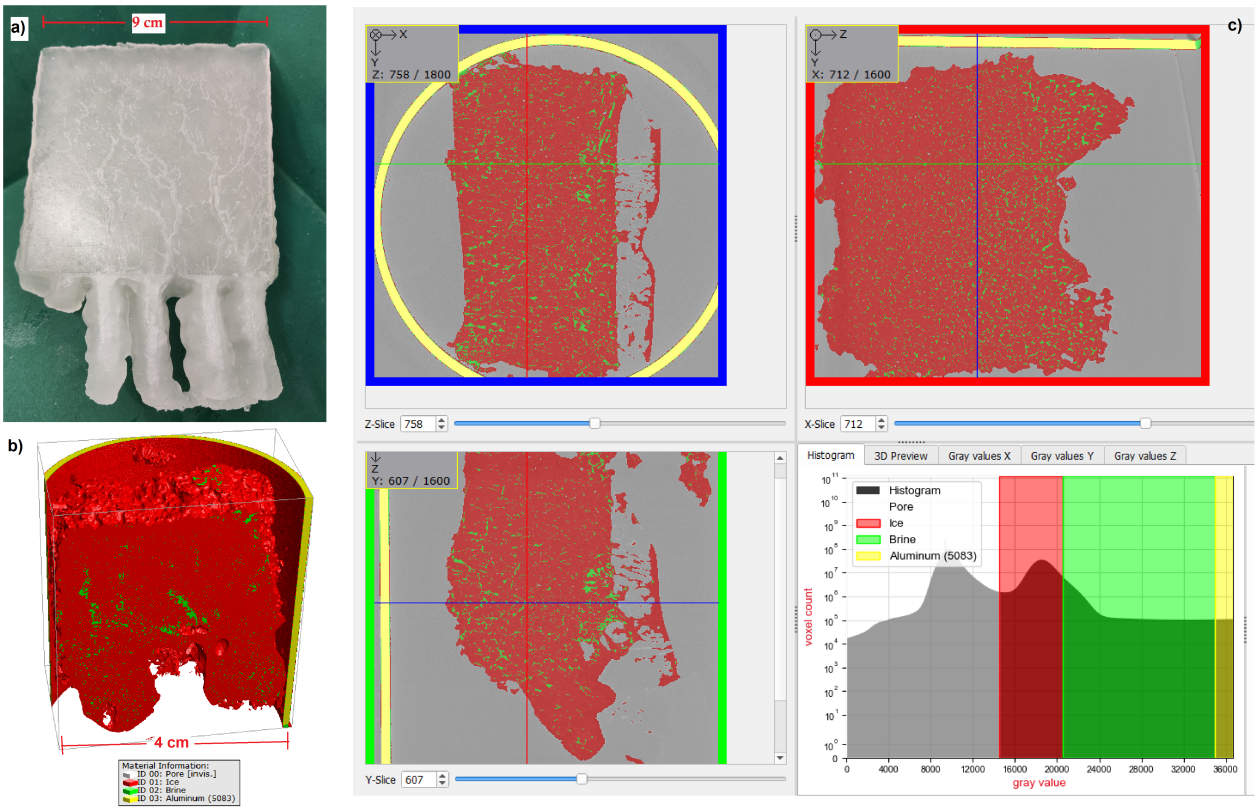

Figure 4: a) Photography of spray ice sample, facing the ice alumina interface with brine channels connected to outflow stalactites; b) half 3D micro-CT image view in half alumina holder; c) example of segmentation of a histogram into ice (here red), air (grey), brine (green) and the alumina holder (yellow) viewing slices from three directions.

RESULTS

The experiments discussed here were run for 2 hours with the cold room set to $T_a = -10$ °C, resulting in a final average spray ice thickness in the range 1 to 3 cm. For all accretion plate sizes (3 to 12 cm) the thickness was decreasing from typically 0.3-0.5 cm at upper part of the plates to

1.5 to 2 cm at the lower part. For the large plate the range was 2 to 4.5 cm. In the present paper we only focus on the spray ice on the lower and thicker half of the accretion plates, and compare the microstructure and properties of spray ice for 4 samples (3 x 3 cm, 6 x 6 cm, 12 x 12 cm, large plate). At the lower end of the accretion plates we frequently observed outflow stalactites as shown in Fig. 4. As discussed further below, these are typically spaced by 1-2 cm, and for the 3 cm samples only one stalactite is found, or it is missing at all. A summary of the other basic properties of spray ice samples from four different accretion plate sizes is given in Table 1 in in columns from left to right: air temperature T_a, ice salinity S_i, ice temperature T_i (only measured for the large plate), open air porosity $\phi_{a,op}$, total brine porosity ϕ_b, closed air porosity $\phi_{a,op}$, median open air pore diameter $D_{a,op}$ (in brackets largest 10%), median open and closed brine pore width $D_{b,op}$ and $D_{b,cl}$, salinity difference of sea spray and sea spray ice ΔS and the salinity loss from drained open pores $\Delta S_{a,op}$ to be discussed below.

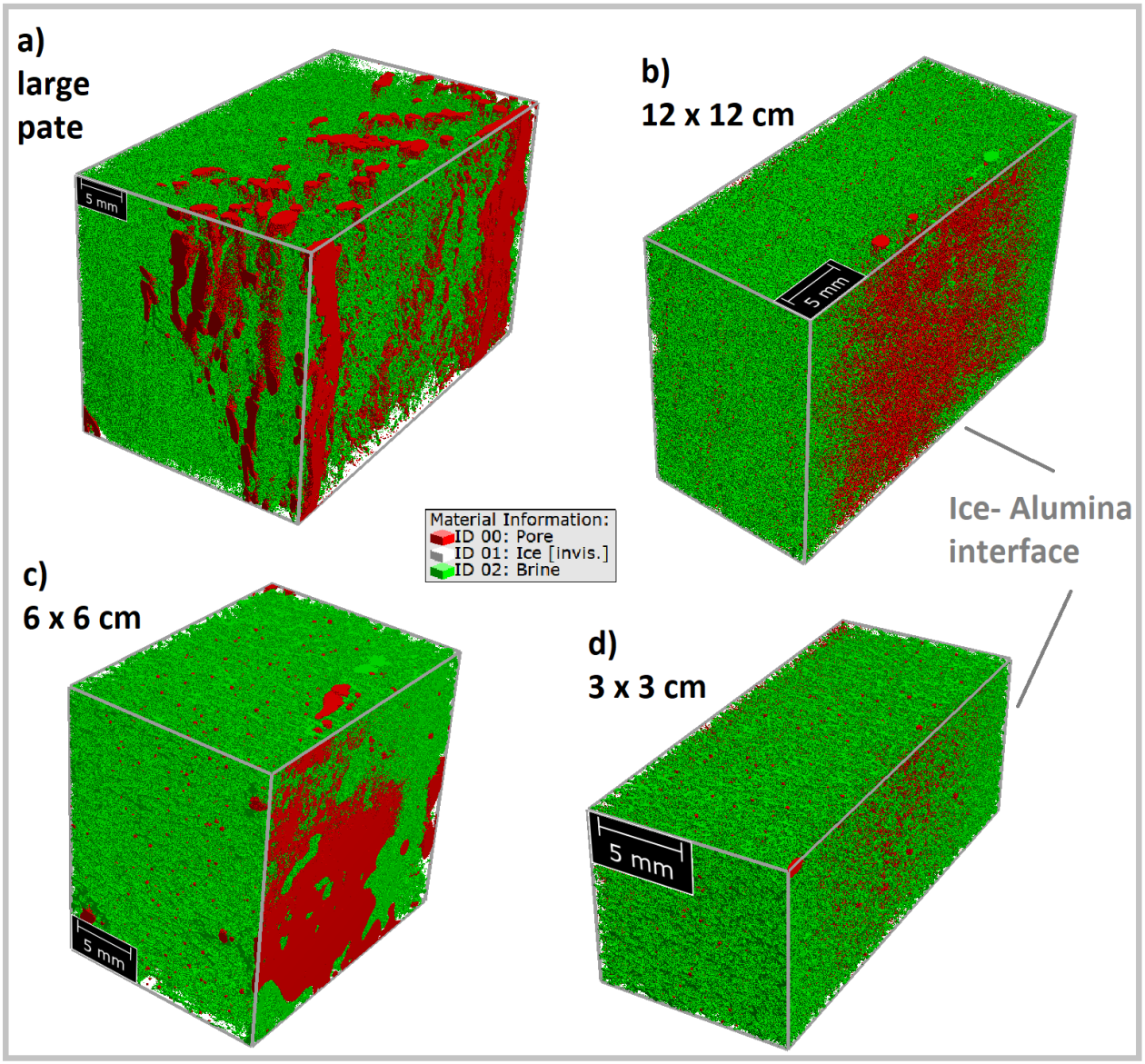

Figure 5: 3D views of the microstructure of saline spray ice grown on 4 accretion plate sizes a) large plate, b) 12 x 12 cm, c) 6 x 6 cm, d) 3 x 3 cm. Brine pores are green, air pores red and ice is invisible. The growth direction is from the front right surface (close to the ice-alumina interface) to the back left surface.

Pore sizes and their distribution

Figure 5 compares 3D views of the microstructure of the different samples, with brine pores in green, air pores in red and ice being invisible. The largest air pore fractions are seen at and close to he ice-alumina interface (front right surface). Further into the sample, and also at the interface (in a),

one observes large air pores with a diameter of a millimeter. These are most dominant for the large plate (a), and almost absent in the 3 x 3 cm sample along the growth direction. At some locations one also finds brine pores of similar diameter, yet not running vertically through the samples. The large air pores resemble pores from which the brine has drained.

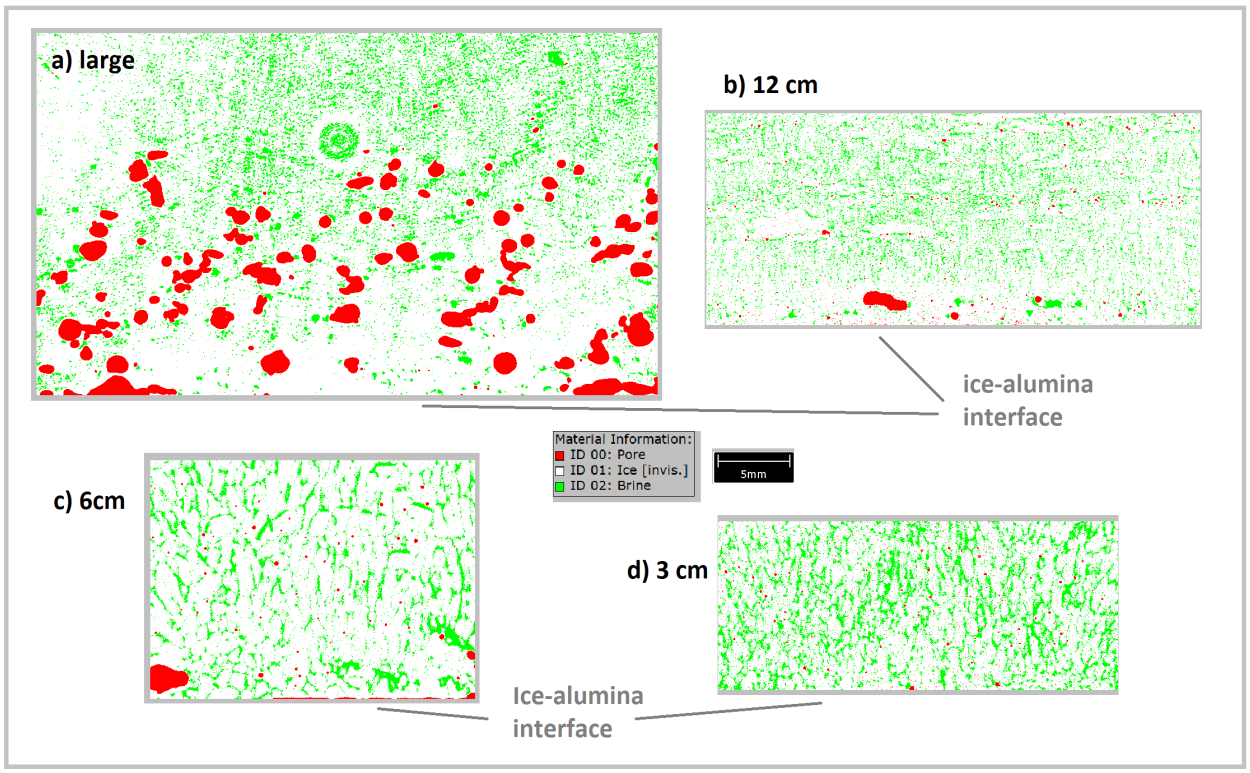

Figure 6: Selected horizontal sections of the 3D images shown in Figure 5.

Figure 6 shows selected horizontal 2D views of the 3D images in Figure 5, illustrating the brine and air pore pattern in the drainage direction. It is seen that, at the ice-alumina interface (drained) air channels are dominating over brine channels. In the vicinity of the drained air channels one sees little brine, indicating that the surrounding brine has formed a wide pore prior to drainage. 6a shows two one prominent feature of wide brine channel with high solid fraction around (in white), that has not yet drained, but illustrates the state prior to drainage. In the 3 cm sample (d) the large channels have not developed yet. It seems however, that also here the air pores are surrounded by regions of low brine concentration. Profiles of brine and air porosity as well as solid volume fraction presented in Figure 7 demonstrate further aspects of the air pore drainage. For the large plate (a) with many drained air pores near the interface the high air porosity correlates with low brine porosity - the source for drainage. For the 3 x 3 cm sample (d) the brine porosity is lower at the ice-alumina interface, indicating that some brine has already been lost here, though not through large drainage channels.Most profiles show a high solid fraction near the interface, with lower values (and thus high drained or undrained salinity) in the center.

The different stages of brine drainage are further underlined by the pore size distribution of open air pores in Figure 8. For the large plate (a) almost no pores with diameters less than 0.3 mm exist, while for the 3 cm plate pores larger than this value have not yet developed. The 6 and 12 cm plate samples show a broader pore size distribution with both regimes present.

Average properties: salinity, porosity and pore size

Ice salinity S_i (column 4 in table 1) is seen to decrease with sample size, with the largest decrease for the large plate. The corresponding difference $\Delta S = S_w - S_i$ from the initial salinity of sea spray $S_w = 34$ ‰ is given in column 11, increasing from 7.8 (3 cm plate) to 17.8 (large plates)

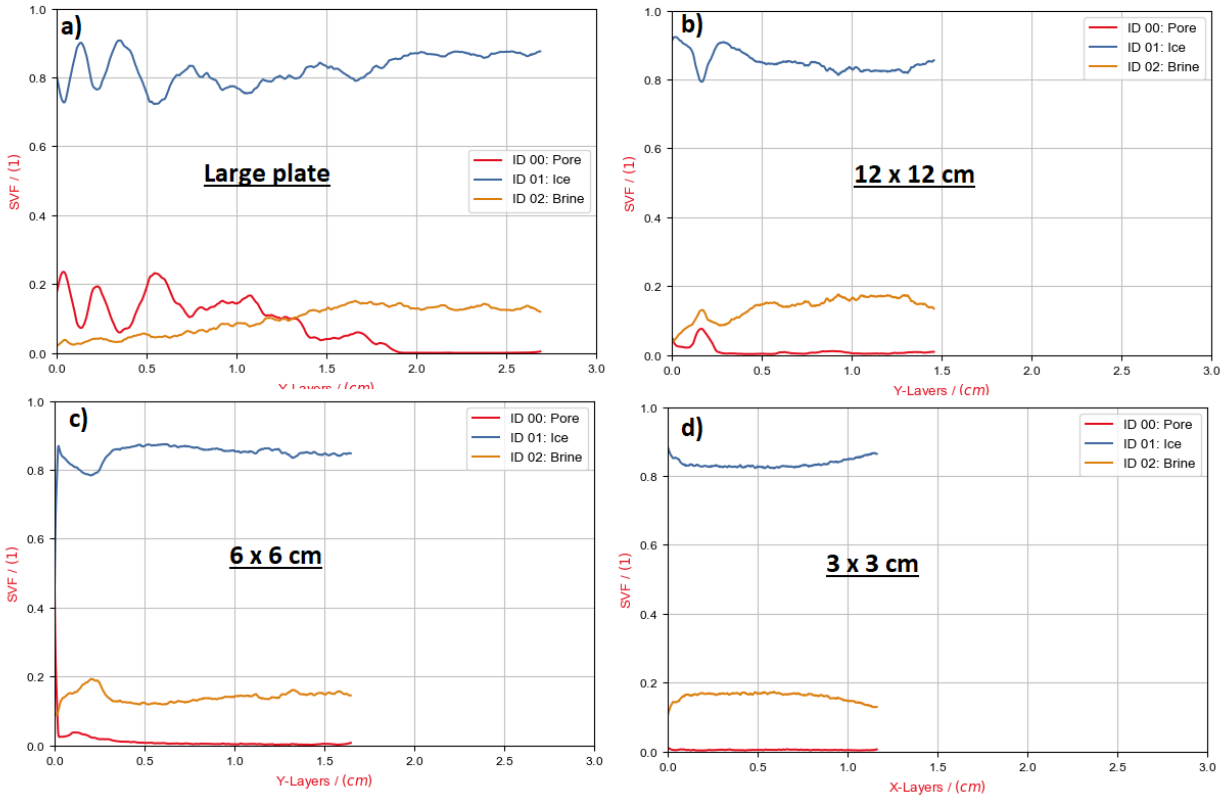

Figure 7: Profiles of brine and air porosity and solid fraction for the 4 accretion plate sizes a) large plate, b) 12 x 12 cm, c) 6 x 6 cm, d) 3 x 3 cm. The distance is measured from the ice-alumina interface at 0 cm.

with sample size. The respective drained air porosity ($\phi_{a,op}$) is increasing from 0.5 to 7.9 %, while the brine porosity (ϕ_b) decreases from 15.9 to 9.6 %. This is consistent with a transition from brine pores to drained air pores with sample size. In the last column we have computed the salinity change corresponding to the drained air pores, assuming an average temperature $T_i = -5.5$ °C as observed for the large scale experiment, as $\Delta S_{a,op}$. This value increases from 0.06 to 7.8 ‰ while the sample size increases from 3 cm to the large plate. As brine drainage is likely taking place before full drainage it should be viewed as a lower estimate of salinity loss due to internal brine drainage. We recall that these data are from the lower part of the plates with thicker spray ice. However, the salinity shows little difference between the lower and upper part.

In column 9 to 11 we give characteristic pore sizes based on size distributions as in Figure 8. The median open air pore diameter $D_{a,cl}$ is similar for the 6 cm, 12 cm and large plate ice, around 0.8 mm. This value also appears as the largest 10 % value (given in brackets) for the 3 cm samples. Brine pores, open and closed, show much smaller diameters. Note that all brine values are close to the resolution limit of two times the voxel size (Nyquist theorem). The true open brine pore diameters are probably smaller.

DISCUSSION

To investigate salt entrapment in saline spray ice we have performed laboratory ice growth experiments, followed by 3D micro-CT imaging of the pore space (brine and air). Our main result is that the existence of drained brine pores depends on sample size and thickness. While spray ice accreted on the smallest (3 x 3 cm) alumina plate has lost 1/4 of the salt of the sea spray from which it has grown, at least another 1/4 is lost from larger samples, when large drainage channels, of order of a millimeter in diameter are established, and drained. The large drainage pores are not found directly at the air-ice interface, yet 1 to 2 cm away from it, and show a tendency to form at the ice-alumina interface.

The drained air porosity in the large plate sample is 7.9 %. Other large spray ice samples

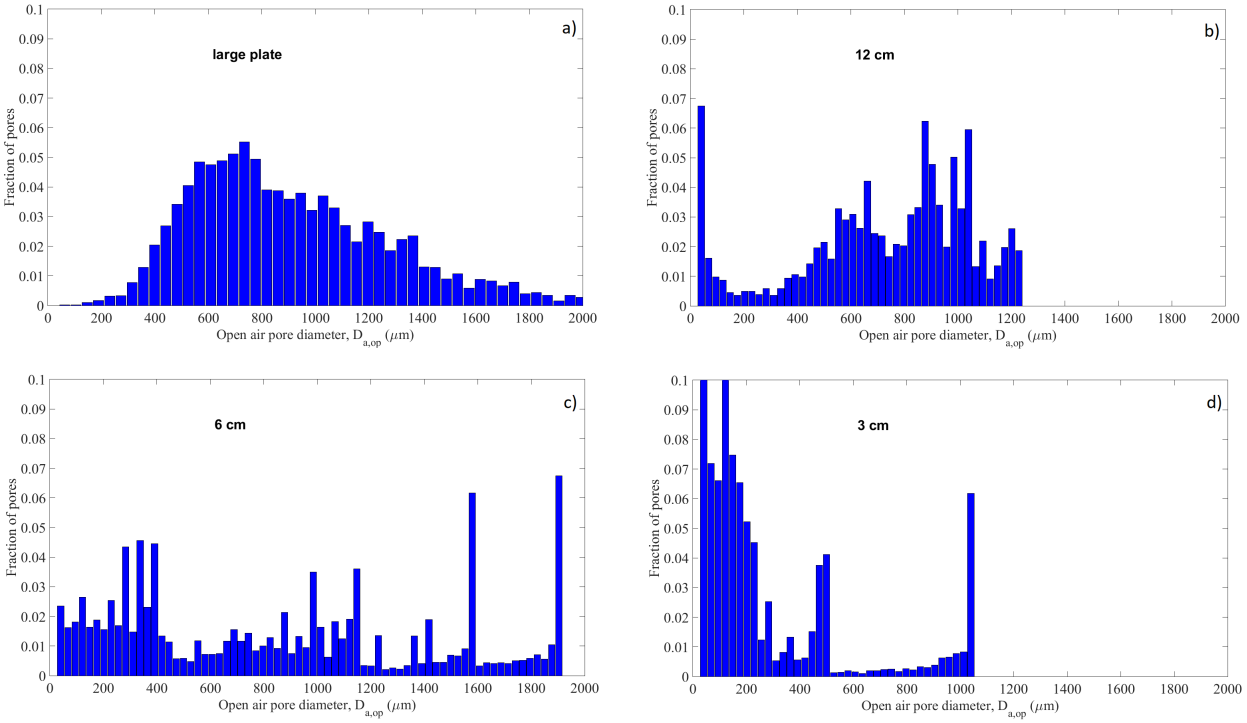

Figure 8: Pore size distributions of open air pores for the 4 different plates sizes.

grown in our tank (not shown here) show similar values. These are at the lower end of observed air porosities for spray ice in the range of 5 to 25 % based on density measurements (Ono, 1964; Ryerson and Gow, 2000). Hence, also other observations are consistent with the formation of large air pores due to brine drainage from the ice interior. The amount of air/drained brine is likely related to several factors like temperature, sample age and thickness.

To explain the observed size dependence of brine drainage we consider several aspects. The first is that the onset of convection in porous media generally depends on a critical Rayleigh Number that is proportional to $\propto KH$, where H is sample height and K is permeability Nield and Bejan (2006). This critical Rayleigh number will be easier reached for large sample plates. As the permeability of a circular brine channel with diameter D is $K \propto D^2$, the pore diameter is the second important property. If, due to larger surface to volume ratio, sea spray freezes faster on small plates, this would likely lead to smaller crystal and pores sizes, and further delay the onset of convection. In addition there needs to be a process that leads to the coarsening of brine channels on short time scales. For this we consider brine expulsion as the relevant process. The increase in solid fraction during cooling of sea spray ice leads, due to the ice-brine density difference, to expulsion of brine. With heat losses normal to the ice-air interface, expulsion may facilitate a path of brine that is first directed into the ice and (latest at the ice-alumina interface) leaves through the sides, top, or bottom. Vertically oriented channels and gravity would favour downward transport, consistent with the growth of stalactites. If brine expulsion is linked to a temperature increase (brine salinity decrease) in the direction of movement this will increase pore sizes by internal melting. Such an increase is expected and observed (of order 1 °C over 2 cm thickness for the present experiments). The process of brine expulsion potentially also involves a size effect, as larger pores may form in ice volumina.

Regarding the brine film movement at the surface, the present experiments do not allow us to make quantitative statements. However, we regard it has likely that internal flow processes play a major role for the loss of brine, whereas flow in a surface brine film mostly redistributes the sea spray and leads to vertical thickness gradients in spray ice accumulations. We are currently planning time-lapse experiments during growth of sea spray, as well as imaging at high resolution to elucidate the processes of brine channel drainage and surface brine flow.

CONCLUSIONS

We have presented and discussed 3D microstructure observations of saline spray ice to better understand its freezing and desalination process. Our main conclusions are
1. We find a size effect in the salinity of sea ice accreted on plates of different size.
2. Salinity decrease with size is linked to drained brine channels that form in larger samples.
3. We propose that the size effect is associated with a combination of convective stability, brine expulsion and redistribution during internal freezing, and temperature gradients.
4. The microstructure data indicate that brine flow from the ice interior, rather than in a surface brine film, is the main controlling process for the desalination of sea spray ice.
5. The present data are of coarse resolution and obtained after 2 hours of ice growth. Time-lapse imaging, and micro-CT scanning with higher spatial resolution are the next steps towards a model for the desalination of sea spray ice. This will improve predictions of ice accretion rates, yet also help to understand the adhesion strength of sea spray ice, as discussed in a companion paper Rübsamen-von Döhren et al. (2023).

ACKNOWLEDGMENTS

We thankfully acknowledge funding of MICROSPRAY, (No 308786) by RCN Norway and Equinor.

REFERENCES

Blackmore, R., Lozowski, E., 1998. A theoretical spongy spray icing model with surficial structure. Atmos. Res. 49, 267–288.

Blackmore, R., Makkonen, L., Lozowski, E., 2002. A new model of spongy icing from first principle. J. Geophys. Res. 107, D21.

Cnudde, V., Boone, M., 2013. High-resolution x-ray computed tomography in geosciences: a review of the current technology and applications. Earth-Science Rev. 123, 1–17.

Dehghani-Sanij, A., Dehgani, S., Naterer, G., Muzychka, Y., 2017. Marine icing phenomena on vessels and offshore structures: Prediction and analysis. Ocean Eng. 143, 1–23.

Desrues, J., Viggiani, G., Besuelle, P., 2006. Advances in X-ray Tomography for Geomaterials. John Wiley and Sons, 2nd International Workshop on the Application of X-ray CT for Geomaterials (GeoX 2006) held in Aussois, France, on 4-7 October, 2006.

GeoDict, 2012-2022. (Geometric material models and computational preDictions of material properties, www.geodict.com).

Horjen, I., 2013. Numerical modeling of two-dimensional sea spray icing on vessel-mounted cylinders. Cold Reg. Sci. Tech. 93, 20–35.

Kong, W., Liu, H., 2018. Unified icing theory on phase transition of supercooled water on a substrate. Int. J. Heat Mass Transf. 123, 896–910.

Kulyakhtin, A., 2014. Numerical modelling and experiments on sea spray icing. Numerical modelling and experiments on sea spray icing, doctoral thesis at ntnu., NTNU, 338.

Kulyakhtin, A., Tsarau, A., 2014. A time-dependent model of marine icing with application of computational fluid dynamics. Cold Reg. Sci.Tech. 104-105, 33–44.

Lock, G., Foster, I., 1990. Experiments on the growth of spongy ice near a stagnant point. J. of Glaciol. 36 (123), 143–150.

Lozowski, E., Szilder, K., Makkonen, L., 2000. Computer simulation of marine ice accretion. Royal. Soc. Lond. Philos. Trans. Ser. A 358 (1776), 2811–2845.

Makkonen, L., 1984. Atmospheric icing on sea structures. Monograph 84-2, US Army Cold Regions Research and Engineering Laboratory.

Makkonen, L., 1987. Salinity and growth rate of ice formed by sea spray. Cold Reg. Sci. Technol. 14, 163–171.

Maus, S., 2020. The plate spacing of sea ice. Annals of Glaciol. 61 (83), 408–425.

Maus, S., Bahafid, S., Hendriks, M., Jacobsen, S., Geiker, M., 2023. X-ray micro-tomographic imaging and modelling of saline ice properties in concrete frost salt scaling experiments. Cold Reg. Sci. Technol. 208, 103780.

Maus, S., Schneebeli, M., Wiegmann, A., 2021. An x-ray micro-tomographic study of the pore space, permeability and percolation threshold of young sea ice. The Cryosphere 15, 4047–4072. URL https://tc.copernicus.org/articles/15/4047/2021/

Mullins, W. W., Sekerka, R. F., 1964. Stability of a planar interface during solidification of a dilute binary alloy. J. Appl. Phys. 35 (2), 444–451.

Nield, D. A., Bejan, A., 2006. Convection in Porous Media, 3rd Edition. Springer.

Ono, N., 1964. Studies of ice accumulation on ships. part ii. conditions of icing and accreted weights. Low Temperature Science Ser. A A22, 171–181.

Overland, J., Pease, C., Preisendorfer, R., Comiskey, A., 1986. Prediction of vessel icing. J. Appl. Meteor. Climatol. 25, 1793–1806.

Ozeki, T., Kose, K., Haishi, T., Nakatsubo, S., Matsuda, Y., 2005. Network images of drainage channels in sea spray icing by mr microscopy. Magn. Res. Imag. 23, 333–335.

Pringle, D. J., Miner, J. E., Eicken, H., Golden, K. M., 2009. Pore space percolation in sea ice single crystals. J. Geophys. Res. 114 (C12017).

Rübsamen-von Döhren, P., Maus, S., He, J., Zhang, Z., June 2023. Modelling oil entrapment in sea ice on the basis of microtomographic images. Proceedings - Port and Ocean Engineering under Arctic Conditions 27.

Ryerson, C., Gow, A., August 2000. Ship superstructure icing: crystalline and physical properties. Tech. rep., CRREL.

Sackinger, W. M., Feyk, C., Groves, J., Gruol, V., Nordlund, O., August 1987. A study of the bond formed between various coated steele surfaces and sea spray ice. In: Proceedings - Port and Ocean Engineering under Arctic Conditions, Fairbanks, Alaska. POAC, pp. 565–570.

Salomon, M., Maus, S., Pertrich, C., 2021. Microstructure evolution of young sea ice from a svalbard fjord using micro-ct analysis. J. Glaciol. 68 (269), 571–590.

Vefsnmo, S., Horjen, I., Løset, S., August 1987. Time-dependent numerical model for sea spray icing on marine structures. In: Proceedings - Port and Ocean Engineering under Arctic Conditions, Fairbanks, Alaska. POAC, pp. 571–579.

Weeks, W. F., Ackley, S. F., 1986. The growth, structure and properties of sea ice. In: The Geophysics of Sea Ice. Vol. 146 of NATO ASI Series. Plenum Press, pp. 9–164, ed. by N. Untersteiner.

Zakrewski, W., Lozowski, E., August 1987. Ice accretion of wires onboard ship under simulated marine conditions. In: Proceedings - Port and Ocean Engineering under Arctic Conditions, Fairbanks, Alaska. POAC, pp. 605–615.